Available online at www.sciencedirect.com
SCIENCE DIRECT®
Acta Materialia 52 (2004) 1937–1951
Acta MATERIALIA
www.actamat-journals.com

Interphase and intergranular stress generation in carbon steels

E.C. Oliver [a,b,*], M.R. Daymond [a], P.J. Withers [b]

[a] ISIS Facility, CLRC Rutherford Appleton Laboratory, Chilton, Didcot, Oxon OX11 0QX, UK
[b] Manchester Materials Science Centre, University of Manchester and UMIST, Grosvenor Street, Manchester M1 7HS, UK

Received 17 November 2003; received in revised form 17 December 2003; accepted 20 December 2003

Abstract

Neutron diffraction spectra have been acquired during tensile straining of high and low carbon steels, in order to compare the evolution of internal stress in ferritic steel with and without a reinforcing phase. In low carbon steel, the generation of intergranular stresses predominates, while in high carbon steel similar intergranular stresses among ferrite grain families are superposed upon a large redistribution of stress between phases. Comparison is made to calculations using elastoplastic self-consistent and finite element methods.
© 2004 Acta Materialia Inc. Published by Elsevier Ltd. All rights reserved.

Keywords: Internal stress; Plasticity; Neutron diffraction; Ferritic steels; Composites

1. Introduction

In general terms, the internal stresses generated during the plastic deformation of engineering alloys may be attributed to their inhomogeneous mechanical properties. In multiphase materials, the greatest variation in mechanical properties is commonly between the phases, giving rise to interphase stresses [1], while in polycrystalline single phase materials, it is the variation of mechanical responses among differently oriented crystallites which predominates, leading to the development of intergranular stresses [2]. In recent years, neutron diffraction has been applied to the measurement of both of these types of internal stress [3–5]. Rarely, however, have comparative studies been performed in which the influence of reinforcing particles on the generation of intergranular stresses in a matrix phase has been investigated [6,7]. This paper describes such a study, in which the evolution of internal stress is compared in ferritic steels with and without a reinforcing phase.

The importance of internal stresses for the mechanical behaviour of carbon steels has been recognised for a long time, with X-ray diffraction studies by Wilson et al. [8,9] dating back as far as 1964. However, the capability of conventional X-ray diffraction is limited in that it reveals only the stress state close to the specimen surface, which differs from that within the bulk material. The neutron diffraction method overcomes this limitation, due to the considerably greater penetration depth of neutrons in engineering materials (~10 mm for iron, compared to ~10 μm for X-rays of comparable wavelength). Bonner et al. [10], Daymond and Priesmeyer [7] and Tomota et al. [11] have applied this technique to the measurement of internal stresses in mainly pearlitic steels, but not for the comparison of steels containing different cementite volume fractions. In the present study, a low carbon (LC) steel consisting essentially of single phase ferrite is compared to a high carbon (HC) steel with a significant cementite volume fraction. Moreover, the HC steel has a spheroidised microstructure which more readily lends itself to simple modelling than the lamellar structure typical of pearlite. Pang et al. [12] and Tomota et al. [13] have also reported measurements of intergranular strain in low carbon steels. This subject remains of considerable interest; in particular, the origin of large intergranular strains measured by these and other authors [7] transversely to the tensile axis has not been clearly elucidated. We therefore address the issue of intergranular strains in ferrite in some detail, using an elastoplastic self-consistent (EPSC)

* Corresponding author. Tel.: +44-1235-445718; fax: +44-1235-445720.
E-mail address: e.c.oliver@rl.ac.uk (E.C. Oliver).

1359-6454/$30.00 © 2004 Acta Materialia Inc. Published by Elsevier Ltd. All rights reserved.
doi:10.1016/j.actamat.2003.12.035

model as an interpretive tool. We also present a combined analysis using finite element and EPSC models for the prediction of ferrite strains in HC steel.

2. Materials and experimental method

The compositions, in weight percent, were Fe–0.07C–1.0Mn–0.25S–0.05Si for the selected LC steel, and Fe–1.0C–0.35Mn–0.30Si–0.40Cr for the HC steel. Both steels were austenitised at 900 °C for 10 h and oil-quenched to avoid carbide network formation. They were then spheroidised at 700 °C for 10 h and allowed to furnace cool in order to minimise the generation of thermal residual stresses. Micrographs representative of the final microstructures are shown in Fig. 1. The LC steel (Fig. 1(a)) has a ferrite grain size of ~10 μm. There is a small volume fraction of MnS (≈2%), but this is a soft, ductile phase which is not expected to provide any reinforcing effect. In contrast, the HC material (Fig. 1(b)) contains about 20 vol% cementite particles. The micrograph in Fig. 1(b) does not have sufficient contrast to resolve individual ferrite grains, but it was possible to see these under the optical microscope. The grain size is similar to the size of the cementite inclusions – i.e. a few microns; significantly smaller than in the LC steel.

Tensile test specimens were machined with gauge length 50 mm and diameters 6 and 8 mm for the HC and LC steels, respectively. In situ neutron diffraction lattice strain measurements were made during uniaxial tensile loading using the ENGIN strain measurement instrument at the ISIS spallation neutron source, as described in [7]. The instrument has two detector banks which are centred on horizontal scattering angles of ±90°. The detectors measure time-resolved spectra, each Bragg peak being produced by reflection from a different family of grains, oriented such that the $\{hkl\}$ plane normal lies at ±45° to the incident beam (to within a few degrees). The load axis was aligned horizontally at +45° to the incident beam, allowing simultaneous measurement of lattice strains in directions both parallel and perpendicular to the applied load. A boron carbide slit of dimensions 5 mm high, 5 mm wide was used to define the incident beam. Radial collimators in front of each detector bank defined an exit aperture of approximately 1.5 mm. Measurements were made at a series of applied loads, using count times of approximately 45 min. The applied load was held constant during the measurement intervals. Several unloads were performed during each experiment in order to measure the evolution of residual strain as a function of accumulated plastic strain. Macroscopic strain was monitored over a gauge length of 12.5 mm using an extensometer. The diffraction spectra were analysed by single peak fits of individual ferrite hkl reflections and by Rietveld refinement of the complete spectrum, using the GSAS software package [14]. A typical diffractogram for the HC steel is shown in Fig. 2. Scattering from the cementite phase was too weak to allow reasonable single peak fits, but acceptable statistical uncertainties were obtained from the Rietveld refinement. Lattice strains determined by Rietveld refinement without accounting for granular anisotropy have been shown by Daymond et al. [15] to be representative of the bulk polycrystalline elastic response. From the axial and transverse diffraction spectra it was evident that a moderate {1 1 0} fibre texture (maximum pole intensity 1.8 times random) existed in the LC steel but that the HC steel was nearly untextured.

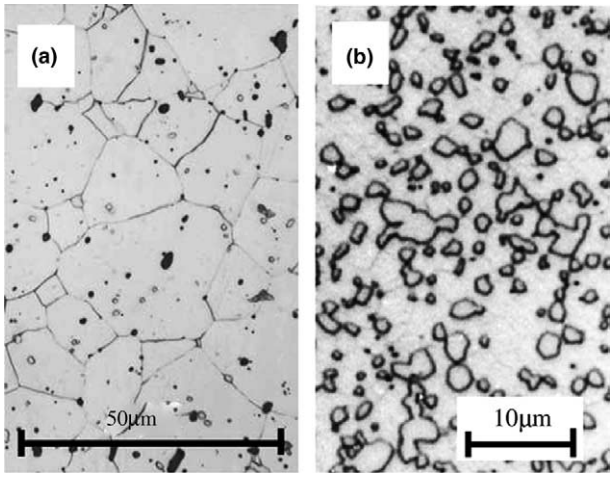

Fig. 1. Optical micrographs of (a) low carbon; (b) high carbon steel.

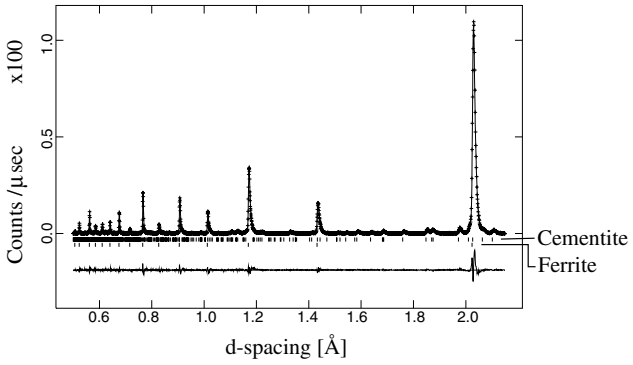

Fig. 2. Typical diffractogram of HC steel: measured datapoints (crosses) and Rietveld refinement (continuous line). Cementite and ferrite peak positions are indicated by markers below the main plot. Also shown below the main plot is the difference curve between the measured spectrum and the Rietveld refinement.

3. Results and discussion

3.1. Macroscopic response

The macroscopic stress–strain curves recorded during neutron data acquisition are shown in Fig. 3. The

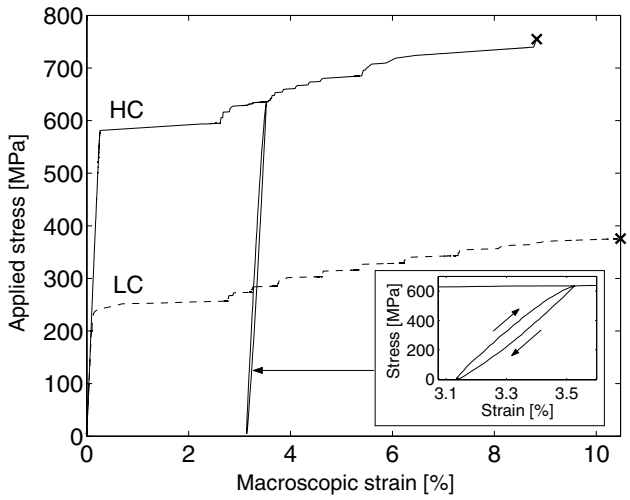

Fig. 3. Macroscopic stress–strain curves acquired during the neutron diffraction experiment. One of several unload–load loops performed on the HC steel is also shown. The inset shows this loop in greater detail.

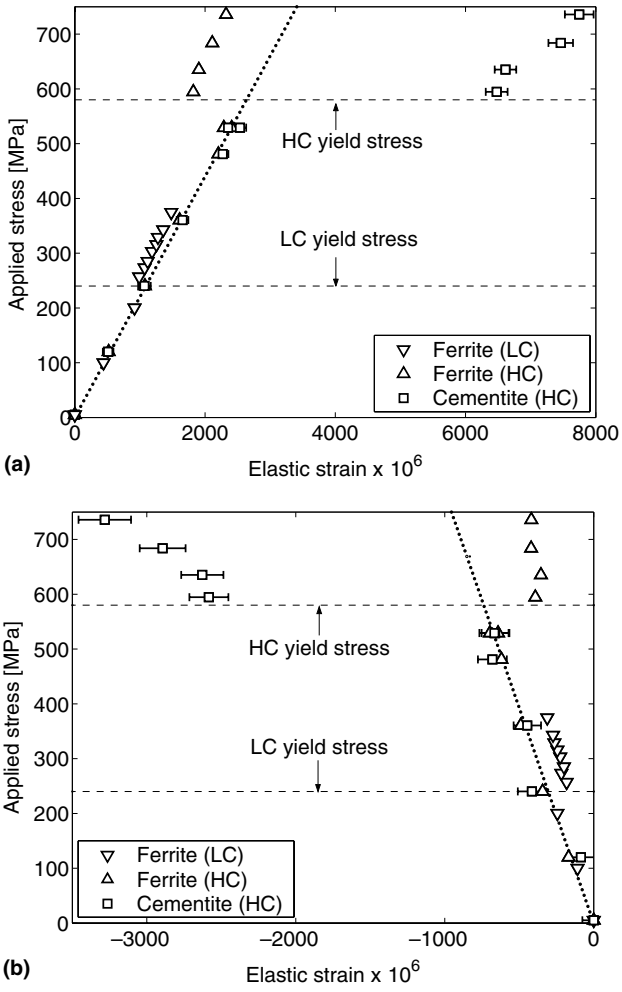

Fig. 4. Lattice strains determined by Rietveld refinement as a function of applied uniaxial tensile stress: (a) axial; (b) transverse strain. The dotted lines passing through the origin are best fits to the initial linear elastic response of the ferrite phase in HC steel. Statistical fitting uncertainties are shown for cementite but are too small to represent for the ferrite phase.

macroscopically determined Young's modulus is 210 GPa for the LC steel and 220 GPa for the HC steel. The HC steel exhibits a substantially greater yield stress than the LC steel. Since the data presented in this and earlier work [10,16] demonstrate that cementite has similiar elastic stiffness to ferrite, the greater yield stress of HC steel is attributed to a smaller grain size rather than to the influence of composite load sharing. Both steels deform initially by Lüders band propagation. This is manifested in the stress–strain curves by the plateaus directly after yielding. Distinct upper and lower yield points are not evident because the tests were performed in load control. Due to the nature of the neutron experiment, the stress–strain curves are composed of a series of steps. The rising edge of each step corresponds to an interval between diffraction measurements when the load was increased; the flat part of the step to a period over which the load was held constant. After holding at load, it was necessary to increase the applied stress by several MPa to continue plastic straining; this suggests that some strain ageing occurs during holding.

3.2. Elastic phase strains

Elastic phase strains measured axially and transversely to the applied load, as determined by Rietveld refinement, are plotted as functions of applied stress in Fig. 4. The reference lattice parameters are taken as those measured prior to loading. For comparison, the responses of the LC and HC steels are shown on the same graphs. In both cases, the responses below the macroscopic yield points are linear, as expected for materials obeying Hooke's Law. In the LC steel, the slope of the axial ferrite response is 213 GPa, in good agreement with the macroscopically determined Young's modulus. The ratio of axial to transverse slopes gives a Poisson's ratio of 0.28. In HC steel, the axial linear elastic responses of both phases have very similar gradients of 220 and 211 GPa for ferrite and cementite, respectively. Moreover, the ratios of axial to transverse slopes are almost the same for both phases: −0.28 for ferrite and −0.29 for cementite. The similarity of the elastic stiffness of ferrite and cementite has been reported by other authors [10,16], and helps to explain why the macroscopic stiffnesses of the LC and HC steels are so similar.

For a single phase material, it is expected that the volume-averaged elastic phase strain should remain linear with applied stress even after the onset of plastic flow, since no redistribution of load between phases is possible. The axial and transverse ferrite responses in the LC steel do indeed remain approximately linear through the yield point, even though 2.5% plastic strain is

introduced between the measurements taken at stresses just below and just above the yield point. There are, however, slight deviations from linearity – a compressive shift of approximately 2.0×10^{-4} in the axial strain and a tensile shift of approximately 1.2×10^{-4} in the transverse strain. Similar shifts have been observed previously and it has been suggested that they are due to axially compressive residual stresses in the diffracting material which are balanced by axially tensile residual stresses in highly distorted regions which fail to diffract, such as dislocation cell walls [8].

The deviations from linearity observed in the LC steel are, however, very small when compared to the shifts observed during yielding of the HC steel. In this case, the axial ferrite response develops a large compressive shift away from the elastic line, while there is a dramatic tensile increase in the cementite axial strain. The transverse strains also change dramatically, the ferrite and cementite transverse strains exhibiting tensile and compressive shifts, respectively.

These changes are consistent with the generation of back stresses in the ferrite matrix as it flows plastically while the cementite inclusions continue to deform elastically. Neglecting any initial residual phase stresses and assuming the phases to be elastically identical and isotropic with Young's modulus 215 GPa and Poisson's ratio 0.28, the volume-averaged axial stresses determined directly after yielding at an applied stress of 595 MPa are 420 MPa in ferrite and 1230 MPa in cementite. Note that just before yielding, the average axial stress was approximately 580 MPa in both phases, owing to the nearly identical elastic constants. Thus the axial stress in the ferrite phase actually falls between the measurements taken before yielding and after Lüders band propagation, even though the applied stress is slightly increased. This demonstrates that the ferrite undergoes a considerable yield point softening. The composite as a whole does not soften to the same extent, because the generation of back stresses provides a source of work hardening.

The gradient of the axial cementite response after yield (110 GPa) is shallower than the gradient beforehand (211 GPa). This indicates that the phase bears an increasing proportion of the applied load as plastic flow continues. That is, back stress hardening continues to operate, increasing the axially tensile residual stress in cementite.

The generation of residual stresses is evident from the elastic strains which remain when the applied stress is removed. In LC steel, residual elastic strains of approximately -2×10^{-4} in the axial direction and 1.5×10^{-4} in the transverse direction develop during Lüders band propagation, and remain approximately constant with further plastic straining. Since these strains are small and consistent with the shifts observed under applied loading, they are not shown graphically here. Fig. 5 shows the development of residual elastic strain with plastic strain in both phases of the HC steel. Two sets of measurements are presented. The unfilled datapoints represent residual strains determined from the measurements made under applied loading, after subtraction of the linear elastic response. The filled datapoints represent the residual strain measurements made after the removal of applied stress. Chronologically, each at-load measurement was recorded directly before the corresponding measurement made after load removal. Although there is some scatter, there is a general trend that the magnitudes of the strains recorded at load are slightly greater than those recorded after the removal of load, by approximately 5–10%. This indicates that some relaxation of interphase stresses occurs during unloading. Support for this statement is provided by close inspection of a typical unloading and re-loading macroscopic response, as shown by the inset in Fig. 3. During unloading, the gradient becomes gradually shallower, suggesting that reverse yielding is activated in regions of matrix where the compressive residual stress is particularly high. This would act to reduce the plastic misfit between phases and lower the residual stresses. During the dwell (~45 min) in the unloaded state, a small amount of further strain recovery develops (~0.01%), suggesting that some time-dependent relaxation also occurs. The re-loading curve begins more steeply than the unloading curve, but forward plasticity is evident several hundred MPa below the previously attained stress.

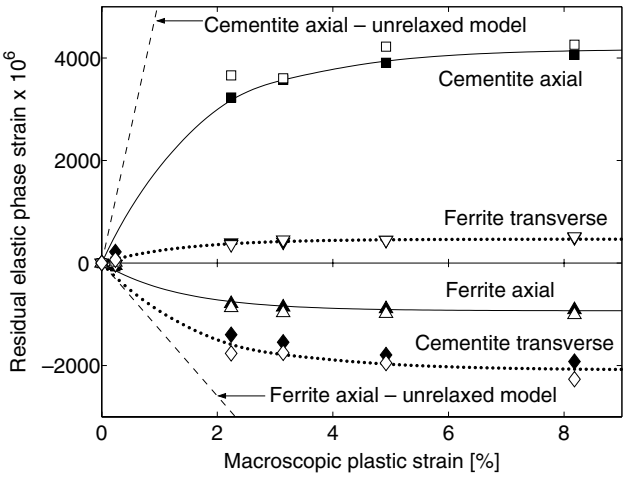

Fig. 5. Residual elastic phase strains in ferrite and cementite phases of HC steel, versus macroscopic plastic strain. Unfilled datapoints are residual strains calculated from measurements at applied load, filled datapoints are direct measurements after load removal. Dashed lines show the axial strains predicted by an unrelaxed mean field model. The solid lines are curves fitted through the axial (filled) datapoints, to serve as guides to the eye. The dotted lines show the transverse residual strains predicted from these curves using a multiplicative factor of −1/2. For clarity, error bars are not shown; typical strain uncertainties are 1.5×10^{-4} for cementite and 2×10^{-5} for ferrite.

As noted, however, the interphase strain magnitudes fall by only a small proportion during unloading, and substantial residual strains remain after unloading. Large, axially tensile and transversely compressive strains develop in the cementite inclusions, balanced by axially compressive and transversely tensile strains in the ferrite matrix. Taking the same elastic constants for both phases and applying stress balance, pairs of ferrite and cementite datapoints are consistent with a cementite volume fraction of between 18% and 22%. This is in good agreement with the value determined by Rietveld refinement, which is 19%. Although the Lüders band propagation precluded measurements at low plastic strains, it is clear from the measurements at 2.2% plastic strain and subsequently that there is an initially high rate of change of residual strain with plastic strain, but that saturation occurs after a few percent plastic strain. This agrees well with results of other authors [9]. The cementite axial residual strain saturates at approximately 4×10^{-3}. Much greater cementite elastic strains have previously been reported in steels with different morphologies [10,11]. Moreover, the changes during unloading suggest that plastic relaxation mechanisms are operative in the HC steel studied here. These observations suggest that saturation occurs because of plastic relaxation operating in the matrix rather than other possible causes such as cementite plasticity, particle fracture or interface damage.

The residual strains can be compared to those calculated from a simple model based upon the mean field method [17,18]. Assuming homogeneous, isotropic elasticity, a plastic misfit strain $\epsilon^{\mathrm{P}}_{ij}$ between matrix and inclusions, and that the cementite inclusions are randomly distributed, elastically deforming spheres, the average matrix and inclusion residual strains, $\langle \epsilon_{ij} \rangle_{\mathrm{M}}$ and $\langle \epsilon_{ij} \rangle_{\mathrm{I}}$, respectively, are calculated as

$$\langle \epsilon_{ij} \rangle_{\mathrm{M}} = -f \frac{(7-5\nu)}{15(1-\nu)} \epsilon^{\mathrm{P}}_{ij}, \tag{1}$$

$$\langle \epsilon_{ij} \rangle_{\mathrm{I}} = (1-f) \frac{(7-5\nu)}{15(1-\nu)} \epsilon^{\mathrm{P}}_{ij}, \tag{2}$$

where ν is the Poisson's ratio and f is the inclusion volume fraction. The conditions of axial symmetry and volume constancy imply that the plastic misfit strain tensor averaged over the matrix has the form

$$\epsilon^{\mathrm{P}}_{ij} = \epsilon^{\mathrm{P}} \begin{pmatrix} -1/2 & 0 & 0 \\ 0 & -1/2 & 0 \\ 0 & 0 & 1 \end{pmatrix}, \tag{3}$$

where ϵ^{P} is a scalar and the tensile axis is taken parallel to the coordinate frame 3-axis. If the matrix plastic strain is assumed to be uniform and completely unrelaxed, then ϵ^{P} is given in terms of the macroscopic plastic strain ϵ^{mac} by

$$\epsilon^{\mathrm{P}} = \frac{\epsilon^{\mathrm{mac}}}{(1-f)}. \tag{4}$$

Assuming a Poisson's ratio of 0.28 and a cementite volume fraction $f = 0.2$, both determined from the diffraction data, the axial residual strains predicted using this unrelaxed assumption are shown in Fig. 5 as dashed lines. For comparison to the experimental data, curves are fitted through the axial (filled) datapoints, to serve as guides to the eye, shown by solid lines. The initial slopes of the fitted experimental curves are of comparable magnitudes but slightly shallower than the gradients predicted by the unrelaxed model. However, as plastic strain increases, the measured strains begin to saturate and are therefore increasingly overestimated by the model predictions.

Whatever its origin (e.g. local matrix plastic flow or cementite plasticity), saturation indicates that the misfit between phases does not continue to grow linearly with plastic strain. Nevertheless, since the origin of the misfit is plastic deformation which conforms to volume constancy, Eq. (3) correctly describes the form of the average misfit even if ϵ^{P} is no longer proportionally related to the macroscopic strain by Eq. (4). Thus, even when relaxation operates, the following relations should hold between the axial and transverse residual strains, $\epsilon_{\parallel}$ and $\epsilon_{\perp}$, respectively:

$$\langle \epsilon_{\perp} \rangle_{\mathrm{M}} = -\frac{1}{2} \langle \epsilon_{\parallel} \rangle_{\mathrm{M}}, \tag{5}$$

$$\langle \epsilon_{\perp} \rangle_{\mathrm{I}} = -\frac{1}{2} \langle \epsilon_{\parallel} \rangle_{\mathrm{I}}, \tag{6}$$

where $\langle\,\rangle_{\mathrm{M}}$ denotes the average in the matrix phase, and $\langle\,\rangle_{\mathrm{I}}$ the average in the cementite inclusions. These predictions are tested in Fig. 5 by multiplying the fitted axial strains (solid lines) by −1/2. The resulting transverse strain predictions, shown by dotted lines, do indeed pass very close to the measured transverse strains.

3.3. Ferrite intergranular strains

In the following, the term "grain family" refers to the subset of grains which contribute to a particular diffraction reflection along a certain scattering direction. That is, the axial hkl grain family comprises all grains in which an $\{hkl\}$ plane normal lies parallel to or within a few degrees of the tensile axis. Similarly, the transverse hkl grain family comprises all grains in which an $\{hkl\}$ normal lies within a few degrees of the transverse scattering vector. Note that the axial and transverse families for a given hkl reflection are composed of different grain subsets. In particular, while all grains in an axial family have a similar orientation with respect to the tensile axis, the grains in a transverse family have a wide range of crystallographic directions aligned axially.

The average elastic strains in 110, 200, 310 ferrite grain families are plotted against applied stress in Fig. 6 (filled datapoints). These families have been chosen because they cover the range of observed behaviours. Consider firstly the slopes of the responses in the elastic regime. For a grain family having $\langle hkl \rangle$ aligned axially, the resolved stiffness depends upon the cubic elastic anisotropy factor $A_{hkl} = (h^2k^2 + k^2l^2 + l^2h^2)/(h^2 + k^2 + l^2)^2$, where for ferrite, greater A_{hkl} implies greater stiffness [19]. Thus we expect the stiffnesses of the axial grain families to increase in the order 200, 310, 110, since A_{hkl} evaluates to 0.00, 0.09, 0.25, respectively, for these families. This trend is clearly seen in the HC steel (Fig. 6(c)), and is also evident in LC steel (Fig. 6(a)), although in this case the 200 and 310 slopes are not well resolved.

For a randomly oriented ferrite polycrystal, greater A_{hkl} also implies a steeper transverse strain response (smaller magnitude Poisson strain for given applied stress). This trend is seen in the HC steel (Fig. 6(d)), although the LC data (Fig. 6(b)) is rather too noisy to establish the trend reliably. However, it should be emphasised that the simple dependence of transverse slope on A_{hkl} is *only* valid for randomly oriented polycrystals, and that in fact the average response of some transverse families is highly sensitive to texture. This is discussed further in Section 4.1.

The yield stresses of the LC and HC steels are indicated in Figs. 6(a)–(d) by horizontal dashed lines. After yielding, the axial grain family responses in the LC steel (Fig. 6(a)) diverge to a greater extent than in the elastic regime. This can be interpreted in terms of load partitioning in similar fashion to the origin of interphase strains. That is, as some grain families begin to yield, those which continue to deform elastically must bear greater load. Thus, the elastic strain response of a grain family which yields early will exhibit a compressive shift relative to the linear elastic regime response, while that of a family which yields late will exhibit a tensile shift. In this case, compressive shifts are seen for the 110 and 310 families, while the 200 response remains approximately linear, indicating that this family yields relatively late compared to the other two. In accounting for this, elastic anisotropy should be considered in addition to plastic anisotropy. That is, a contributory reason to the late yielding of the 200 family is that it bears less stress in the elastic regime, being the elastically most compliant family. This is discussed further in Section 4.1.2.

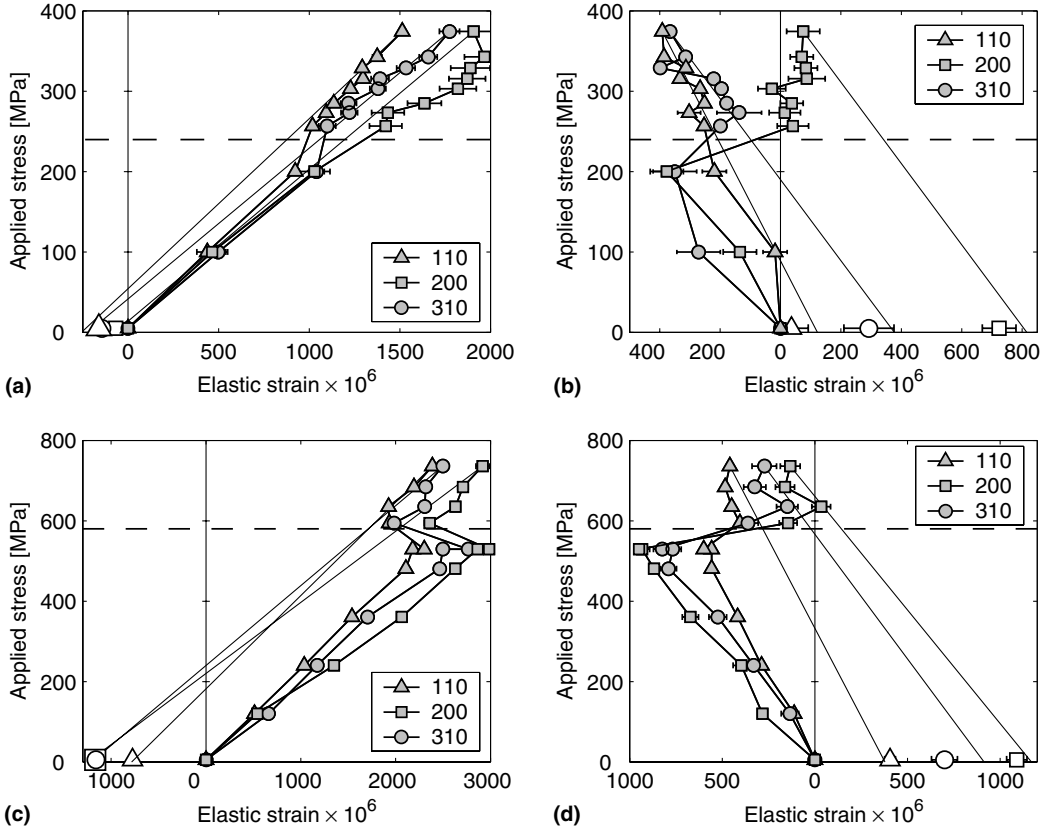

Fig. 6. Average ferrite grain family elastic strains, plotted against applied stress (filled datapoints). Unloading responses expected for purely elastic unloading are shown by the straight lines extrapolating the datapoints at highest applied stress to zero stress. The actual strains measured after load removal are shown by unfilled datapoints. For the maintenance of clarity, error bars – which represent fitting uncertainties – are excluded from some datapoints. (a): LC, axial; (b): LC, transverse; (c): HC, axial; (d): HC, transverse.

Yield point shifts of much greater magnitude are observed in the strains measured transversely to the tensile axis (Fig. 6(b)). The 110 transverse response remains approximately linear through the yield point, but the 310 transverse strain develops a tensile shift during yielding, while the 200 transverse strain develops a particularly dramatic tensile shift of approximately 5×10^{-4}. This indicates that for grains in which a $\langle 200 \rangle$ direction lies transversely, a large component of tensile residual stress develops along this transverse direction. Such a shift has been previously reported for ferrite [7,12] but a simple explanation has not been given. We address this point in Section 4.1.3. Interestingly, similar shifts have also been observed for the 200 transverse family in fcc polycrystals [5]. Although different slip systems operate in the two crystal structures, our analysis in Section 4.1.3 demonstrates that these observations are in fact related. Beyond the yield point, the 200 transverse response is approximately vertical, indicating that the tensile internal stress along the transverse $\langle 200 \rangle$ direction continues to increase with further plastic straining.

The residual strains measured after the final loading step are also shown in Figs. 6(a)–(d), as unfilled datapoints. Also shown, as thin straight lines, are the unloading responses expected for purely elastic unloading (the gradients for which are found by straight line fitting to the initial elastic regime responses). Extrapolating these responses to zero applied stress, it is seen that in general the measured strains are close to those expected for elastic unloading. In comparison to the intergranular strains which develop in alloys of other crystal structures, e.g. titanium (hcp) [20], the axial residual strains in the LC steel are notably small (magnitude $< 2 \times 10^{-4}$ for all families). However, the transverse residual strains are much larger than the axial strains, corresponding to the large shifts observed during yielding.

In the axial response of the HC steel, all of the ferrite grain family strains exhibit a compressive shift during yielding. This is of course due to overall load transfer to cementite. The relative magnitudes of the shifts are of interest, however. The compressive shift is greater for the 200 than the 110 family. After unloading, the 200 family has the more compressive residual strain. In contrast, in the LC steel the 110 strain develops the more compressive shift during yielding, and the more compressive residual strain after unloading.

In the transverse direction, however, trends in yield point shifts and residual strains for the HC steel are similar to those for LC steel. All families exhibit a tensile shift due to the introduction of transversely tensile residual phase stress, but the shift is by far the greatest for the 200 family and smallest for the 110 family, in good agreement with the trend seen in the LC steel. Correspondingly, the tensile residual strain is greatest for the 200 and smallest for the 110 family.

To clarify the similarities and differences, the grain family residual strains generated in the two steels after approximately 5% plastic deformation are plotted together in Fig. 7 (these do not correspond exactly to the final residual strains plotted in Fig. 6, since these were acquired at different plastic strains for the two samples). For a direct comparison of intergranular strains, the average phase strains as determined by Rietveld refinement have been subtracted. This shows that the trend in the axial intergranular residual strains in the LC steel is almost completely reversed in the HC steel, but that the trend among the transverse strains is the same for both steels. This apparent conflict is resolved by consideration of the combined effect of elastic anisotropy and the average phase stresses. In the HC steel, the ferrite is in a state of axially compressive residual stress. Since 200 is the most compliant axial grain family, this stress produces the greatest compressive residual strain in this family. This competes against the effect of plastic misfit among grain families which, as seen from the LC data, results in the *most tensile* residual strain in the 200 family. However, since the intergranular strains produced by grain-to-grain misfit are small, it appears that the interphase effects dominate, explaining why the trend in intergranular strains is reversed relative to that in LC steel. In the transverse direction, however, the interphase stress merely accentuates the trend due to intergranular misfit. Since 200 is the most compliant family, the transversely tensile phase stress produces the most tensile residual strain in this family, which adds to the large tensile strain developed due to intergranular misfit.

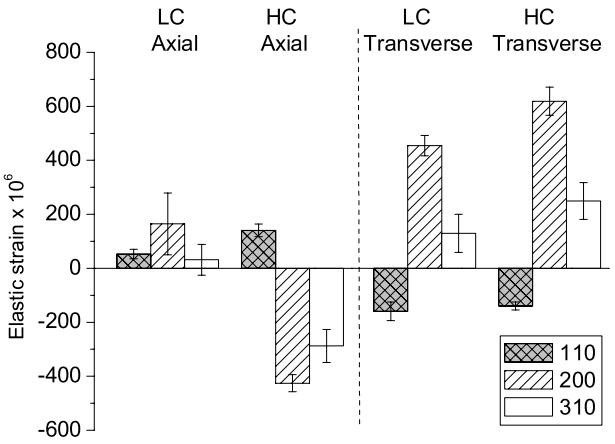

Fig. 7. Ferrite grain family intergranular residual strains, after subtraction of the phase-averaged residual strain, for LC and HC steels, at plastic strains of approximately 5% (exact plastic strains: LC 5.15%, HC 4.29%).

4. Modelling of internal stress development

4.1. Intergranular stress in single phase ferrite

The EPSC model first proposed by Hill [21] has proved successful in predicting intergranular strains in polycrystals of different crystal structures [4,12,20]. In this section, we describe EPSC simulations conducted using the implementation written by Turner and Tomé [22], which is based upon the formulation of Hutchinson [23]. The objective is to rationalise some of the observed trends in intergranular stress development in ferrite. Specifically, we present simulations which help to explain the relatively small tensile and large transverse elastic strains which are developed among ferrite grain families.

The EPSC model is described in detail elsewhere [22,23], and therefore only a brief description is given here. The polycrystalline aggregate is represented by a discrete set of grain orientations, which are attributed volume fractions to match the observed crystallographic texture. Grains are attributed the single crystal elastic constants and slip properties characteristic of the material under study. They are regarded as ellipsoidal inclusions embedded within a homogeneous effective medium which has the average properties of all grains. The stress/strain response of each grain orientation to a small increment of macroscopic stress or strain is estimated from the elastic Eshelby solution for the response of an ellipsoidal inhomogeneity. Since the properties of the medium derive from the average response of all grains, the calculation proceeds iteratively. The full aggregate response is calculated by solving for many stress/strain increments, taking account of single crystal hardening. The model is a small strain formulation, in which no grain rotation is incorporated.

For this work, we have used ferrite elastic stiffness constants taken from the literature [24]: $C_{11} = 237$, $C_{12} = 141$, $C_{44} = 116$ GPa, with corresponding compliance components $S_{11} = 0.0076$, $S_{12} = -0.0028$, $S_{44} = 0.0086$ GPa^{-1}. We have assumed all grains to be spherical. In bcc crystals, the slip direction is unambiguously $\langle 1\,1\,1\rangle$, but there are many possible slip planes within the $\langle 1\,1\,1\rangle$ zones [25,26]. We have assumed slip on $\{1\,1\,0\}$, $\{1\,1\,2\}$, $\{1\,2\,3\}$ planes but, as demonstrated by Hutchinson [23], if the number of slip planes is large enough and they are well distributed about the slip direction, the model should be insensitive to the planes explicitly specified. Moreover, we have assumed isotropic hardening of slip systems. The model formulation becomes unstable if negative hardening is specified and hence the yield point softening and Lüders elongation inherent to the LC steel cannot be simulated in the model. Therefore, since the fine details of the macroscopic response cannot be captured, a simple linear hardening law has been assumed, parameterised by

$$\mathrm{d}\tau^i = \theta \sum_j \mathrm{d}\gamma^j, \tag{7}$$

where $\mathrm{d}\tau^i$ is the increment in the threshold shear stress on the ith slip system, θ is the hardening rate, and $\mathrm{d}\gamma^j$ is the shear strain increment on the j system.

In order to represent the moderate $\{1\,1\,0\}$ fibre texture of the LC steel, the initial axial and transverse spectra were fitted in GSAS using a spherical harmonic texture model, assuming axial symmetry [14]. A discrete population of 3066 weighted orientations was generated from the estimated texture using the popLA software package [27]. The average lattice strain of the axial $h\,k\,l$ family was calculated as the elastic strain resolved along the tensile axis, averaged over all grain orientations having a $h\,k\,l$ plane normal lying within 5° of the axial direction. For the transverse lattice strains, the axial symmetry was exploited to gain better statistical averaging. This is important because application of the model immediately reveals that the average transverse strains are particularly sensitive to the exact grain population. A specific transverse direction was not specified. Instead, the transverse $h\,k\,l$ family strain was taken as the elastic strain resolved along the projection of the $h\,k\,l$ plane normal onto the transverse plane, averaged over all grain orientations having an $h\,k\,l$ normal lying within 5° of the transverse plane. This method allows the transverse strain to be evaluated using a much larger sample of grain orientations.

4.1.1. Model validation

In order to assess the ability of the EPSC model to reproduce the intergranular strains observed experimentally, the model macroscopic response was firstly fitted to the LC steel flow curve using the initial threshold shear stress τ_0 (assumed the same for all slip systems and grains) and hardening rate θ as fitting parameters. The flow curve resulting from this procedure is shown in Fig. 8(a) together with the experimental curve. Although the post-yield plateau is not captured, the calculated macroscopic stiffness is in excellent agreement with the experimental stiffness, and the stress–strain response is well captured at large plastic strains. Having fitted the macroscopic curve, the model predictions for average grain family elastic strains were compared to the measured strains. The results are shown in Fig. 8(b). Agreement is generally very good, considering the simplicity of the hardening law used.

In the axial direction, the slopes of the initial linear elastic responses are reasonably well reproduced. The model effectively captures the compressive yield point shifts from linearity of the 110 and 310 responses. The final gradients of the responses are also consistent with the experimental data. The model 200 response is most interesting in the low plastic region, where unfortunately datapoints could not be acquired. Nevertheless, the

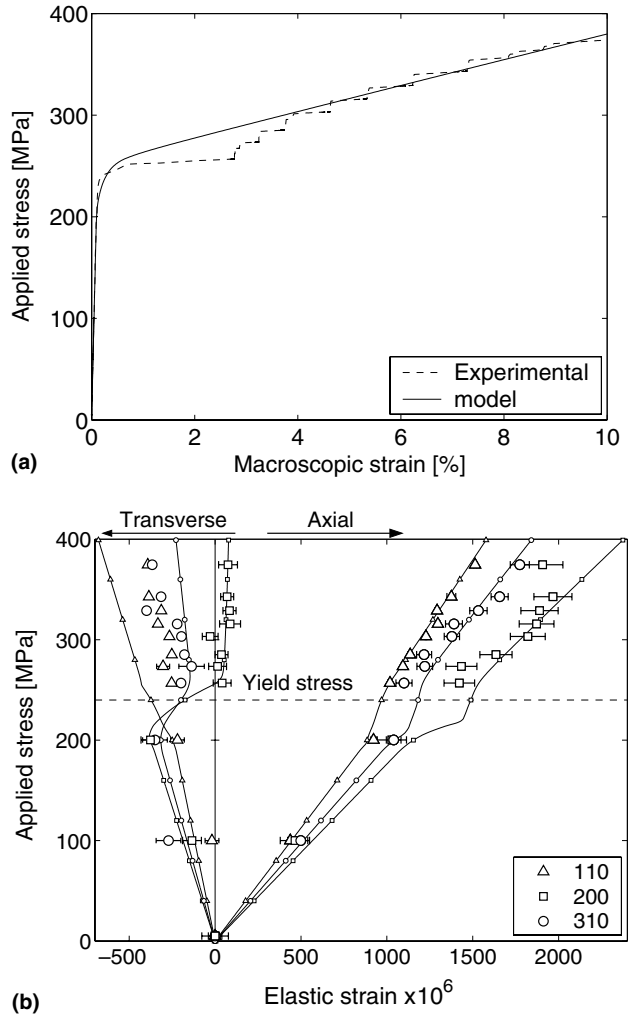

Fig. 8. Comparison of EPSC simulation of LC steel to experimental data: (a) modelled and experimental macroscopic stress–strain curves; (b) modelled and experimental evolution of average grain family elastic strains, against applied stress. In (b), experimental measurements are represented by large datapoints, model calculations by continuous lines joined by small datapoints.

response is in good agreement with the experimental data at higher applied stresses.

In the transverse direction, the large tensile shift and subsequent near-vertical gradient of the 200 response are reproduced particularly well. The positive shift of the 310 response is also well captured although the model predicts too steep a gradient after the yield point shift. The response of the 110 transverse family is least well reproduced; the model predicts a negative shift while the observed response remains approximately linear through yield.

Since the model captures most of the major experimental trends, we can be confident of its predictive ability, and thus use it to gain further insight into the generation of intergranular strains in ferrite. Application of the model in this manner is described in the remainder of this section.

4.1.2. Influence of elastic anisotropy

The model results support the assertion made from the experimental data that the axial residual strains which develop in single phase ferrite are small, at least in comparison to the transverse strains. It has been noted above that a competition between elastic and plastic anisotropy may be in part responsible for this. The EPSC model may be used to investigate this by simulating a bcc polycrystal composed of grains which have the same plastic properties used in the previous simulation, but which are elastically isotropic. This is achieved by setting the single crystal compliance components according to

$$S_{11} = \frac{1}{E}, \quad S_{12} = -\frac{v}{E}, \quad S_{44} = \frac{2(1+v)}{E}, \tag{8}$$

where E and v are the Young's modulus and Poisson's ratio, respectively. Taking these equal to the macroscopic values determined for LC steel, an EPSC simulation of such an elastically isotropic polycrystal has been performed. For a procedure of 5% tensile straining followed by unloading, the calculation predicts residual elastic strains of +1.61, −2.66, -1.78×10^{-4} for the 110, 200 and 310 axial grain families, respectively. These compare to values of −1.54, +0.82, -1.60×10^{-4}, respectively, calculated for the elastically anisotropic polycrystal. Thus it is seen that the removal of elastic anisotropy almost completely reverses the trend in intergranular strain generation: in the absence of elastic anisotropy, the 200 family develops the most compressive residual strain, while the 110 family develops a tensile residual strain. This demonstrates that grains in the 200 axial family are among the most favourably oriented for slip while grains in the 110 axial family are among the least favourably oriented, as supported by Taylor model calculations, which show that the Taylor factor is close to minimum for the 200 family and close to maximum for the 110 family [28]. However, since in the real elastically anisotropic polycrystal the latter grains bear more stress within the elastic regime, they in fact reach yield at lower applied macroscopic stress. Thus it appears that elastic and plastic anisotropy do indeed tend to influence intergranular strain development in opposite ways, and therefore that their coupling tends to reduce the magnitude of axial intergranular strains in ferrite.

4.1.3. Transverse strains

As noted above, members of a transverse grain family may have a range of orientations with respect to the tensile axis. However, the diffraction method gives only the resolved elastic strain averaged over all of the relevant grain orientations (although additional information about the distribution of strains is available from analysis of the peak profile). The EPSC model may, however, be used to evaluate the response of individual

grains, and therefore to investigate the strains developed among different members of a grain family. This can be achieved systematically by adding grains of specific orientations to the grain population, but attributing zero weight to these orientations so that they do not influence the average properties of the embedding medium. Using this strategy, the EPSC-determined transverse strains developed in specific (elastically anisotropic) grains spanning the range of possible orientations of the 110 and 200 transverse families are shown in Figs. 9(a) and (b), respectively. In Fig. 9(a), all grain orientations have a common $\langle 1\,1\,0\rangle$ transverse direction, along which the strain is resolved. They differ in their rotation about this direction, characterised by the angle θ_1 – as illustrated by the inset. θ_1 varies from 0° when $\langle 2\,0\,0\rangle$ lies axially to 90° when another $\langle 1\,1\,0\rangle$ direction lies axially. In Fig. 9(b), the common transverse direction along which the strain is resolved is $\langle 2\,0\,0\rangle$ and the grains are rotated about this direction by an angle θ_2, also illustrated by an inset. θ_2 varies from 0° when $\langle 2\,0\,0\rangle$ lies axially to 45° when $\langle 1\,1\,0\rangle$ lies axially.

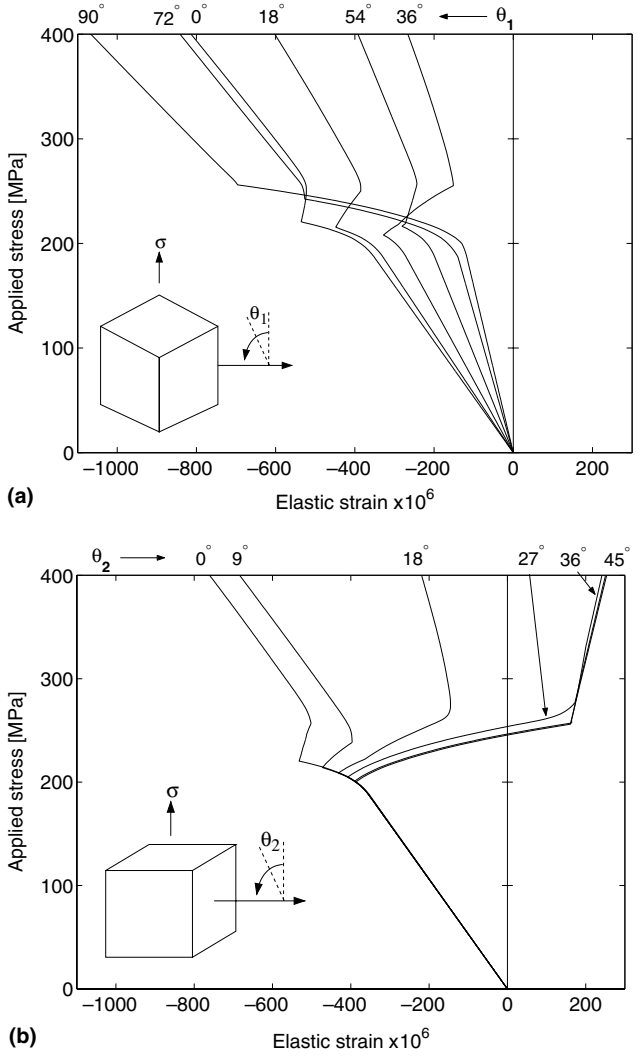

Fig. 9. EPSC simulations of transverse lattice strain development with applied stress in ferrite grains of specific orientations: strain resolved along (a) $\langle 1\,1\,0\rangle$ and (b) $\langle 2\,0\,0\rangle$ transverse directions, for various rotations θ_1 and θ_2, respectively, about these directions. The insets illustrate these rotations.

A difference which is immediately apparent between Figs. 9(a) and (b) is that the elastic regime slopes vary considerably among members of the 110 transverse family, but not at all among members of the 200 family. This result may be rationalised by considering the elastic strain response of a single crystal. If a uniaxial stress σ is applied to a cubic crystal along a unit vector $[l,m,n]$, then the elastic strain $\epsilon_\perp$ developed along a unit vector $[u,v,w]$ perpendicular to $[l,m,n]$ is given by

$$\frac{\epsilon_\perp}{\sigma} = S_{12} + \left[S_{11} - S_{12} - \frac{1}{2}S_{44}\right]F, \tag{9}$$

where S_{ij} is the elastic compliance tensor in contracted matrix notation and F is a factor given by

$$F = (l^2u^2 + m^2v^2 + n^2w^2) \tag{10}$$

[29]. If $[u,v,w] = [1,0,0]$, then $F = 0$ for all possible $[l,m,n]$. That is, the transverse strain developed along a $\langle 1\,0\,0\rangle$ direction is independent of the direction perpendicular to this along which uniaxial stress is applied. In fact, this result has been shown to be generally true in any crystal structure for an axis which possesses n-fold rotational symmetry, where $n > 2$ [30]. If however $[u,v,w] = 1/\sqrt{2}[1,1,0]$, then F varies in the range $0 \leqslant F \leqslant 1/2$, and the extremes of Eq. (9) are

$$\epsilon_\perp/\sigma = S_{12} = -2.8 \times 10^{-12}\ \text{Pa}^{-1} \tag{11}$$

when $[l,m,n] = [0,0,1]$, and

$$\epsilon_\perp/\sigma = \frac{1}{2}\left[S_{11} + S_{12} - \frac{1}{2}S_{44}\right] = +0.22 \times 10^{-12}\ \text{Pa}^{-1} \tag{12}$$

when $[l,m,n] = 1\sqrt{2}[1,-1,0]$. Surprisingly, depending upon the direction of the tensile axis, the transverse strain developed along $\langle 1\,1\,0\rangle$ can be either negative or positive. In a polycrystal, each grain is constrained by the surrounding medium. As seen from Fig. 9(a), this modifies the $\langle 1\,1\,0\rangle$ transverse strains so that they are always negative, but they still show considerable variation depending upon the orientation relative to the tensile axis. This has some practical importance: the effective Poisson's ratio of the 110 family will as a consequence be particularly sensitive to crystallographic texture, and this must be appreciated if errors are not to be made in the evaluation of residual stresses based upon measurements of the 110 diffraction peak. Data given by Pang et al. [12] support this assertion: they measured elastic strain responses in textured ferritic steel plate, subjected to uniaxial stress along the plate rolling direction. The initial slopes of the lattice strain–stress responses measured along the plate normal and transverse directions differed by approximately 17% for the

{2 2 0} reflection but by no more than 10% for any of the other reflections measured (200, 112, 222). Evaluating Eqs. (11) and (12) for other materials, it is found that the ⟨1 1 0⟩ transverse strain also varies between positive and negative depending upon the tensile axis orientation for single crystals of a number of other cubic alloys including stainless steel, nickel and copper. Thus caution should be exercised when using the 110 diffraction peak to evaluate residual stresses in a whole range of common engineering materials.

Upon plastic straining, different members of the 110 transverse family respond in markedly different ways. The strain response of the grain having $\theta_1 = 0°$ remains approximately linear, except for a slight deviation in the early stage of plasticity. As θ_1 increases, the lattice strain responses exhibit tensile shifts relative to the elastic regime responses. However, as θ_1 increases further, the shifts become compressive. The greatest compressive shift is seen in the orientation with $\theta_1 = 90°$, when the tensile axis is parallel to a ⟨1 1 0⟩ direction. This is also the orientation with the steepest response in the elastic regime. Since different members of the family develop shifts of different senses, the trend in the average response – whether tensile or compressive – is very sensitive to the exact distribution of grain orientations. Since the grain population applied in the EPSC model only approximately represents the texture of the real material, it is unsurprising that it does not reproduce the 110 transverse response accurately.

In the 200 transverse family however, with the exception of the orientation having $\theta_2 = 0°$, which remains approximately linear, all members exhibit tensile shifts. This explains why apparently all authors report large tensile 200 transverse residual strains, regardless of texture [7,12]. The magnitude of the shift increases rapidly as θ_2 increases from 0°, but saturates so that the responses with $\theta_2 = 27°$ and $\theta_2 = 45°$ are almost identical. Thus the magnitude of the shift is large for the majority of grains contributing to the 200 transverse reflection. This accounts for the large average residual strain, as observed in the diffraction measurements.

It is straightforward to understand why large residual strains develop in grains of some orientations but not in others. Consider two spherical grains, denoted A and B, whose orientations are shown schematically in Fig. 10. Also marked on the schematics are the four ⟨1 1 1⟩ slip directions, and the external reference frame, in which the tensile direction is parallel to the 3-axis. Let us assume that the average plastic strain among all grains (equal to the macroscopic plastic strain) is axially symmetric, given in the external reference frame by

$$\overline{\epsilon^{\mathrm{P}}}_{ij} = \epsilon^{\mathrm{P}} \begin{pmatrix} -1/2 & 0 & 0 \\ 0 & -1/2 & 0 \\ 0 & 0 & 1 \end{pmatrix}. \tag{13}$$

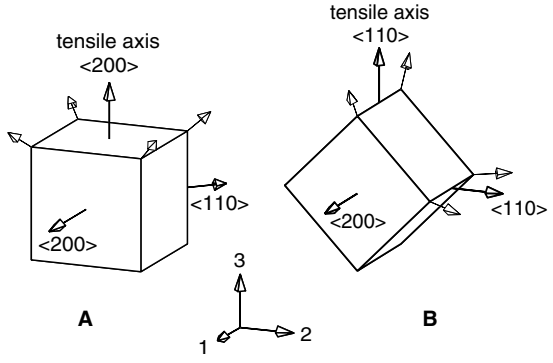

Fig. 10. Orientations of two ferrite grains, denoted A and B. Unlabelled arrows show the four ⟨1 1 1⟩ slip directions. The tensile axis is parallel to the reference frame 3-axis.

Moreover, as justified by the small magnitude of the measured axial residual strains, let us assume that all grains develop the same axial plastic strain, ϵ^{P}. In grain A, the tensile axis is parallel to a ⟨2 0 0⟩ direction and the four ⟨1 1 1⟩ slip directions are symmetrically distributed about this direction. If we assume the same threshold shear stress on all slip systems, it is clear by symmetry that in this grain the plastic strain is axially symmetric, and thus equal to the macroscopic plastic strain, $\overline{\epsilon^{\mathrm{P}}}_{ij}$. Thus on average there is no misfit between grains of type A and the embedding medium. Choosing the transverse scattering vector parallel to the labelled ⟨1 1 0⟩ direction, grain A corresponds to the 110 transverse family member with $\theta_1 = 0°$. Alternatively, if the transverse scattering vector is chosen parallel to the labelled ⟨2 0 0⟩ transverse direction, the grain corresponds to the 200 member with $\theta_2 = 0°$. Thus the lattice strain responses of these members remain approximately linear through yield.

In grain B, the tensile direction lies parallel to a ⟨1 1 0⟩ direction. In this case, two of the ⟨1 1 1⟩ slip directions lie perpendicular to the tensile axis (and thus have zero Schmid factor) and the other two lie perpendicular to the ⟨1 1 0⟩ transverse direction. Thus plastic strain cannot be accommodated along this direction and the plastic strain tensor of this grain has the form

$$\epsilon^{B}_{ij} = \epsilon^{\mathrm{P}} \begin{pmatrix} -1 & 0 & 0 \\ 0 & 0 & 0 \\ 0 & 0 & 1 \end{pmatrix}. \tag{14}$$

In grains of this orientation, the plastic contraction of the grain along the transverse ⟨2 0 0⟩ direction is thus twice that of the medium as a whole. This misfit must be accommodated by a large tensile elastic strain in this direction. Resolving along this direction, grain B corresponds to the 200 transverse family member with $\theta_2 = 45°$, explaining why the resolved transverse residual strain in grains of this type is large and tensile. Along the ⟨1 1 0⟩ transverse direction, the contraction of the

embedding medium is greater than that of the grain, and the misfit must be accommodated by a large compressive elastic strain. Resolving along this direction the grain corresponds to the 110 member with $\theta_1 = 90°$, accounting for the large compressive shift predicted by the EPSC model in the lattice strain response of this 110 family member.

This analysis also helps to explain why large tensile 200 transverse intergranular strains are also commonly observed in fcc materials. In this case, $\langle 1\,1\,1 \rangle$ is the slip plane normal, rather than the slip direction. With this modification, the arguments made in relation to Fig. 10 remain valid. Clausen [31] has also discussed the effect of non-uniform transverse contraction on the transverse intergranular strains in fcc polycrystals.

To summarise, the analysis presented here demonstrates that large axial residual stresses do not develop in single phase ferrite, but that this does not imply that transverse residual stresses are also small. In fact, these are large because the distribution of slip directions does not facilitate uniform transverse contraction, causing large transverse incompatibilities. This conclusion is similar to that drawn by Pang et al. [32] in relation to zircaloy-2 with rod texture. They measured minimal axial intergranular strains, but strong transverse interactions. This was rationalised by the fact that all grains possess similar orientations relative to the tensile axis, but that the hard *c*-axis direction is distributed randomly within the transverse plane, causing incompatibilities between neighbouring grains in which its direction differs.

4.2. Combined intergranular and interphase stress analysis of HC steel

The application of the finite element (FE) method for modelling of interphase stresses in multiphase materials is well established [1] while, as demonstrated above, the EPSC model provides an instructive tool for examining the generation of intergranular stresses within a single phase. It is natural then to explore the possibility of combining these approaches for the full prediction of internal stresses in multiphase materials, using the FE method for the prediction of bulk phase stresses, and the EPSC model for the intergranular stresses corresponding to these phase stresses. To this end, we have followed a simple strategy for combining the outputs of FE and EPSC models for the prediction of ferrite internal stresses in HC steel. The approach is described in this section and assessed by comparison to the diffraction data acquired for HC steel.

A three-dimensional unit cell FE model was constructed, consisting of a cube containing one quadrant of a spherical inclusion centred at one vertex (volume fraction 20%), surrounded by matrix with perfect bonding at the interface. By imposing boundary conditions to constrain the unit cell to remain cuboidal during deformation, and assigning appropriate constituent properties, the model was taken to be representative of an infinite simple cubic array of cementite inclusions embedded within a ferrite matrix. The inclusions were assigned perfectly elastic behaviour and the matrix elastoplastic behaviour. As supported by the diffraction data, it was assumed that both phases have identical elastic constants, specified as 215 GPa and 0.28 for the Young's modulus and Poisson's ratio, respectively. The matrix was attributed a von Mises yield criterion and linear, isotropic hardening. To account for matrix softening, flow curves were defined at two nominal temperatures. By switching the nominal temperature after initial yielding, upper and lower yield stresses could be introduced. The model was processed using the ABAQUS package.

The following strategy was adopted for combining the FE and EPSC outputs. The matrix upper and lower yield stresses and hardening parameter were used as fitting parameters in the FE model to match the stress–strain response to the experimental flow curve of HC steel. Having determined the matrix properties in this manner, the ferrite single crystal plasticity parameters were varied within the EPSC model such that the EPSC-calculated ferrite flow curve matched that determined from the FE model as closely as possible. The FE output was also used to map the applied uniaxial stress to the triaxial matrix stress. This triaxial stress history was then applied to the EPSC model to predict ferrite intergranular stress as a function of applied stress. The issue of matrix softening presents some difficulties. As noted previously, the present EPSC implementation cannot account for softening. The EPSC-determined flow curve was therefore fitted only to the post-softening part of the FE-determined flow curve. Moreover, due to the softening effect, the mapping of applied stress to matrix stress is not one-to-one. Just prior to yield, the matrix experiences the uniaxial yield stress; after Lüders band propagation, at the same applied stress, the matrix experiences a lower axial stress, as well as a transverse stress component. In order to reflect the two yield point stress states and the change in matrix properties, two separate EPSC simulations were performed. The first run was a purely elastic simulation up to the macroscopic yield stress. In the second run, the matrix was assigned the single crystal plasticity parameters fitted according to the procedure described above.

The results of this approach are shown in Fig. 11. Fig. 11(a) summarises the tailoring of the bulk matrix and single crystal plasticity parameters. The thin, solid line shows the matrix flow curve fitted for the FE model. This has an upper yield stress of 580 MPa, a lower yield stress of 470 MPa, and a subsequent hardening rate of 17.5 MPa/%. Using this matrix behaviour, the FE-calculated macroscopic response of the overall composite

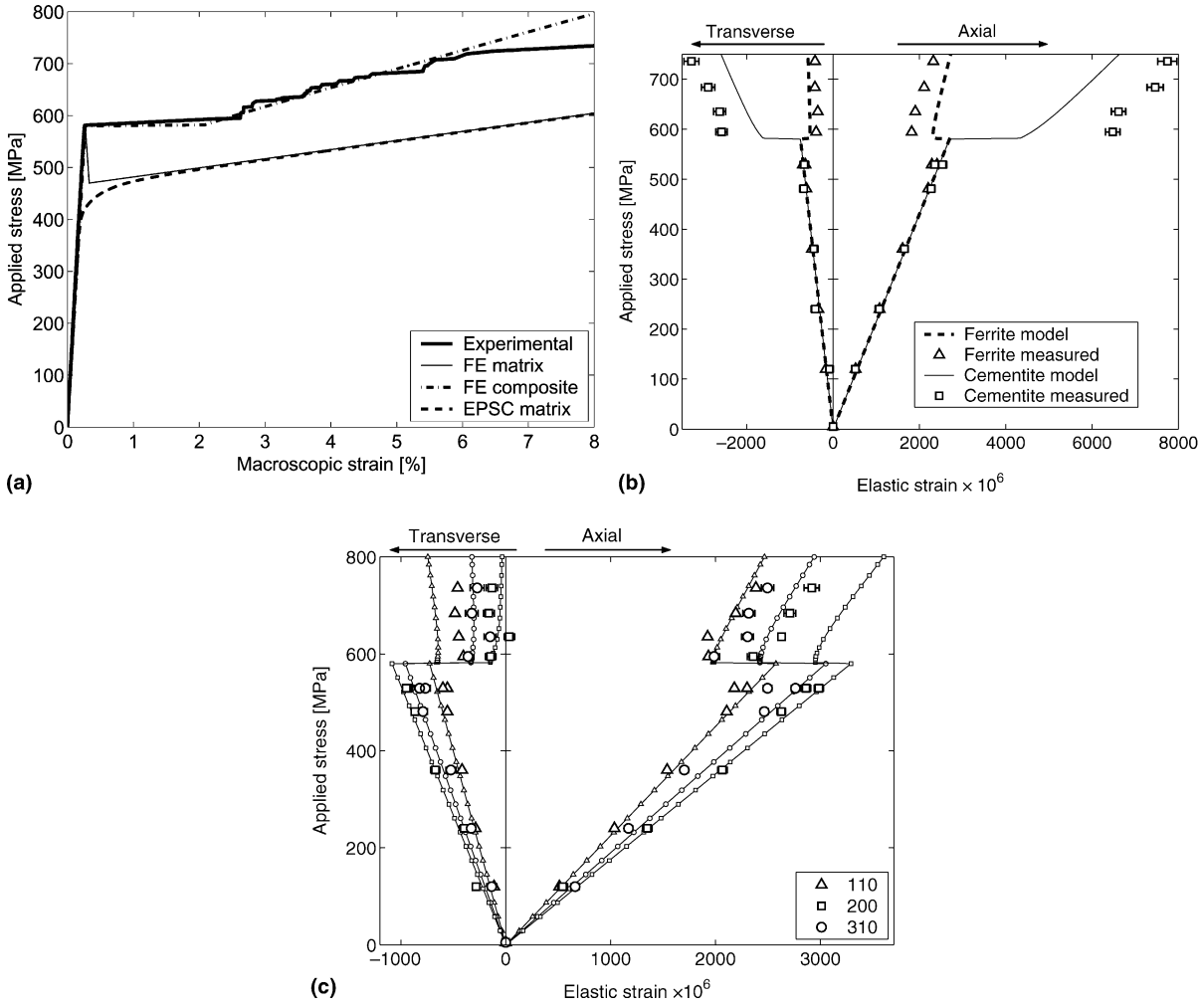

Fig. 11. Combined analysis of internal stresses in HC steel: (a) macroscopic stress–strain curves. The EPSC flow curve (dashed line) is fitted to the FE matrix curve (thin, solid line). This in turn is tailored such that the FE composite flow curve (dot-dashed line) matches the experimental flow curve (bold, solid line). (b) Modelled and experimental volume-averaged elastic phase strains, vs. applied stress. (c) modelled and experimental ferrite grain family elastic strains, vs. applied stress. In (c), experimental measurements are represented by large datapoints, model calculations by continuous lines joined by small datapoints.

under monotonically increasing uniaxial tensile stress is shown by the dot-dashed line. This matches the experimental flow curve (bold, solid line) very well up to 6% strain. In particular, the matrix softening gives rise to a plateau directly after yield, which is well matched to the plateau in the experimental curve. The fitted EPSC ferrite flow curve is shown by the dashed line. As noted above, this cannot capture the initial softening as specified for ferrite in the FE model, but the EPSC flow curve fits the FE matrix flow curve very closely above 1% strain.

Fig. 11(b) shows the FE-determined volume-averaged axial and transverse elastic phase strains, compared to those measured experimentally. As expected, the initial linear responses are well matched. When yielding occurs, the model qualitatively captures the sense of the lattice strain changes observed experimentally. The axial ferrite strain develops a compressive shift, and the axial cementite strain a proportionally larger tensile shift. Correspondingly, in the transverse direction, the ferrite strain develops a tensile shift and the cementite a compressive shift. However, in all cases, the predicted shifts are not as great as those observed experimentally. It might be anticipated that the specification of greater matrix softening would increase the magnitudes of these shifts. In practice, this is not the case: the post-yield plateau in the composite flow curve extends to greater plastic strain, but the lattice strain shifts are not significantly altered. This is because the model composite cannot support the imposed load directly after yielding, and must extend considerably so that the matrix may work harden. The introduction of greater matrix softening does not significantly alter the back stresses generated within the composite, but merely requires the model to elongate further in order that the matrix may work harden to a greater extent. Since greater back

stresses can be generated in the real material, this demonstrates the efficacy of a random dispersion of inclusions in constraining matrix flow.

Proceeding to the final stage of the analysis, the predicted evolution with applied stress of ferrite grain family elastic strains is shown in Fig. 11(c), in comparison to the experimental data. In the elastic regime, the slopes are well reproduced. At yield, lattice strain shifts are observed. Considering that the elastic and plastic regimes correspond to different EPSC runs, this is wholly unsurprising; nevertheless, the relative magnitudes of the shifts are of interest. In the transverse direction, the relative magnitudes are in the correct order: the 200 strain exhibiting by far the greatest shift and 110 the smallest. In the axial direction, however, the 200 strain exhibits the smallest shift, which is not the case in the experimental data. Thus the model does not reproduce the effect of elastic anisotropy on the partitioning of strains due to the ferrite back stress, as was discussed in Section 3.3. Generally, however, considering the simplicity of the analysis, its ability to identify the trends of intergranular strain development is encouraging. Therefore it is worth exploring the approach in greater detail. This can be achieved by embedding the EPSC code as a user-defined subroutine within the ABAQUS framework. We are currently developing such a model, which will offer the ability to predict intergranular stresses in composites and geometrically complex engineering components at a relatively low computational expense.

5. Conclusions

Neutron diffraction and modelling have been applied to compare the evolution of internal stresses in LC and spheroidised HC steels during tensile deformation. The principal conclusions of this study are listed below:

1. Ferrite plasticity and yield point softening in HC steel gives rise to the generation of large interphase residual stresses. At low plastic strains, the stresses are consistent with calculations using an unrelaxed mean field model. The interphase stresses relax by approximately 5–10% during unloading and reach saturation after a few percent plastic strain.
2. In the absence of a reinforcing phase, internal stresses in LC steel arise largely due to incompatibilities between differently oriented ferrite grains. Axial intergranular stresses are small but much larger stresses develop transversely to the tensile axis. An elastoplastic self-consistent model has been used to explain these observations; revealing that competition between elastic and plastic anisotropy acts to reduce axial stresses, and that anisotropic contraction causes large transverse incompatibilities. The model has also demonstrated that the average strain response of the 110 transverse grain family is highly sensitive to crystallographic texture.
3. Intergranular stresses are also generated in the ferrite matrix of HC steel. In this case, the average phase stress alters the partitioning of grain family residual strains, due to the effect of elastic anisotropy. A combined approach to the modelling of internal stresses has been presented, coupling the finite element method for interphase stress determination with the elastoplastic self-consistent method for the calculation of intergranular stresses.

Acknowledgements

E.C. Oliver gratefully acknowledges postgraduate support from EPSRC and the Rutherford Appleton Laboratory.

References

[1] Clyne TW, Withers PJ. An introduction to metal matrix composites. Cambridge: Cambridge University Press; 1993.
[2] Clausen B, Lorentzen T, Leffers T. Acta Mater 1998;46:3087.
[3] Fitzpatrick ME, Lodini A, editors. Analysis of residual stress by diffraction using neutron and synchrotron radiation. London: Taylor & Francis; 2003.
[4] Clausen B, Lorentzen T, Bourke MAM, Daymond MR. Mater Sci Eng A 1999;259:17.
[5] Daymond MR, Tomé CN, Bourke MAM. Acta Mater 2000;48:553.
[6] Allen AJ, Bourke MAM, Dawes S, Hutchings MT, Withers PJ. Acta Metall 1992;40:2361.
[7] Daymond MR, Priesmeyer HG. Acta Mater 2001;50:1613.
[8] Wilson DV, Konnan YA. Acta Metall 1964;12:617.
[9] Wilson DV, Bate PS. Acta Metall 1986;34:1107.
[10] Bonner NW, Modlen GF, Webster PJ, Root JH, Holden TM. In: Proceedings of ICRS-5, Linköping, Sweden; 1997. p. 1109.
[11] Tomota Y, Lukáš P, Neov D, Harjo S, Abe YR. Acta Mater 2003;51:805.
[12] Pang JWL, Holden TM, Mason TE. J Strain Anal 1998;5:373.
[13] Tomota Y, Lukáš P, Harjo S, Park J-H, Tsuchida N, Neov D. Acta Mater 2003;51:819.
[14] Larson A, Von Dreele RB, GSAS – General Structure Analysis System. Technical Report LA-UR-86-748, Los Alamos National Laboratory, USA; 1994.
[15] Daymond MR, Bourke MAM, Von Dreele RB, Clausen B, Lorentzen T. J Appl Phys 1997;82:1554.
[16] Umemoto M, Liu ZG, Masuyama K, Tsuchiya K. Scripta Mater 2001;45:391.
[17] Brown LM, Stobbs WM. Philos Mag 1971;23:1185.
[18] Mori T, Tanaka K. Acta Metall 1973;21:571.
[19] Nye JF. Physical properties of crystals. Oxford: Oxford University Press; 1985.
[20] Oliver EC, Daymond MR, Quinta da Fonseca J, Withers PJ. In: Proceedings of MECASENS 2, Manchester, UK; 2003.
[21] Hill R. J Mech Phys Solids 1965;13:89.
[22] Turner PA, Tomé CN. Acta Metall 1994;42:4043.
[23] Hutchinson J. Proc R Soc A 1970;319:247.
[24] Dieter GE. Mechanical metallurgy. 3rd ed. New York: McGraw-Hill; 1986.
[25] Barrett CS, Ansel G, Mehl RF. Trans ASM 1937;25:702.

[26] Opinsky AJ, Smoluchowski R. J Appl Phys 1951;22:1488.
[27] Kocks UF, Kallend JS, Wenk H-R, Rollet AD, Wright SI. popLA, preferred orientation package – Los Alamos. Technical Report LA-CC-89-18, Los Alamos National Laboratory, USA; 1994.
[28] Chin GY, Mammel WL. Trans TMS-AIME 1967;239:1400.
[29] Allen AJ, Hutchings MT, Windsor CG, Andreani C. Adv Phys 1985;34:445.
[30] Oliver EC. The generation of internal stresses in single and two phase materials. Ph.D. thesis, University of Manchester; 2002.
[31] Clausen B. Characterisation of polycrystal deformation by numerical modelling and neutron diffraction measurements. Ph.D. thesis, Risø National Laboratory; 1997. p. 38.
[32] Pang JWL, Holden TM, Turner PA, Mason TE. Acta Mater 1999;47:373.